

Diverse properties of electron Forbush decreases revealed by the Dark Matter Particle Explorer

F. Alemanno,^{1,2} Q. An,^{3,4} P. Azzarello,⁵ F. C. T. Barbato,^{6,7} P. Bernardini,^{1,2} X. J. Bi,^{8,9} H. Boutin,⁵ I. Cagnoli,^{6,7} M. S. Cai,^{10,11} E. Casilli,^{6,7} J. Chang,^{10,11} D. Y. Chen,¹⁰ J. L. Chen,¹² Z. F. Chen,¹² Z.X. Chen,^{12,8} P. Coppin,⁵ M. Y. Cui,¹⁰ T. S. Cui,¹³ I. De Mitri,^{6,7} F. de Palma,^{1,2} A. Di Giovanni,^{6,7} T. K. Dong,¹⁰ Z. X. Dong,¹³ G. Donvito,¹⁴ J. L. Duan,¹² K. K. Duan,¹⁰ R. R. Fan,⁹ Y. Z. Fan,^{10,11} F. Fang,¹² K. Fang,⁹ C. Q. Feng,^{3,4} L. Feng,¹⁰ S. Fogliacco,^{6,7} J. M. Frieden,^{5,*} P. Fusco,^{14,15} M. Gao,⁹ F. Gargano,¹⁴ E. Ghose,^{1,2} K. Gong,⁹ Y. Z. Gong,¹⁰ D. Y. Guo,⁹ J. H. Guo,^{10,11} S. X. Han,¹³ Y. M. Hu,¹⁰ G. S. Huang,^{3,4} X. Y. Huang,^{10,11} Y. Y. Huang,¹⁰ M. Ionica,¹⁶ L. Y. Jiang,¹⁰ W. Jiang,¹⁰ Y.Z. Jiang,^{16,†} J. Kong,¹² A. Kotenko,⁵ D. Kyratzis,^{6,7} S. J. Lei,¹⁰ B. Li,^{10,11} W. L. Li,¹³ W. H. Li,¹⁰ X. Li,^{10,11} X. Q. Li,¹³ Y. M. Liang,¹³ C.M. Liu,¹⁶ H. Liu,¹⁰ J. Liu,¹² S. B. Liu,^{3,4} Y. Liu,¹⁰ F. Loparco,^{14,15} M. Ma,¹³ P. X. Ma,¹⁰ T. Ma,¹⁰ X. Y. Ma,¹³ G. Marsella,^{1,2,‡} M. N. Mazziotta,¹⁴ D. Mo,¹² Y. Nie,^{3,4} X. Y. Niu,¹² A. Parenti,^{6,7,§} W. X. Peng,⁹ X. Y. Peng,¹⁰ C. Perrina,^{5,*} E. Putti-Garcia,⁵ R. Qiao,⁹ J. N. Rao,¹³ Y. Rong,^{3,4} A. Ruina,⁵ R. Sarkar,^{6,7} P. Savina,^{6,7} Z. Shangguan,¹³ W. H. Shen,¹³ Z. Q. Shen,¹⁰ Z. T. Shen,^{3,4} L. Silveri,^{6,7,¶} J. X. Song,¹³ M. Stolpovskiy,⁵ H. Su,¹² M. Su,¹⁷ H. R. Sun,^{3,4} Z. Y. Sun,¹² A. Surdo,² X. J. Teng,¹³ A. Tykhonov,⁵ G. F. Wang,^{3,4} J. Z. Wang,⁹ L. G. Wang,¹³ S. Wang,¹⁰ X. L. Wang,^{3,4} Y. F. Wang,^{3,4} D. M. Wei,^{10,11} J. J. Wei,¹⁰ Y. F. Wei,^{3,4} D. Wu,⁹ J. Wu,^{10,11} S. S. Wu,¹³ X. Wu,⁵ Z. Q. Xia,¹⁰ Z. Xiong,^{6,7} E. H. Xu,^{3,4} H. T. Xu,¹³ J. Xu,¹⁰ Z. H. Xu,¹² Z. Z. Xu,^{3,4} Z. L. Xu,¹⁰ G. F. Xue,¹³ M. Y. Yan,^{3,4} H. B. Yang,¹² P. Yang,¹² Y. Q. Yang,¹² H. J. Yao,¹² Y. H. Yu,¹² Q. Yuan,^{10,11} C. Yue,¹⁰ J. J. Zang,^{10,**} S. X. Zhang,¹² W. Z. Zhang,¹³ Yan Zhang,¹⁰ Y. P. Zhang,¹² Yi Zhang,^{10,11} Y. J. Zhang,¹² Y. Q. Zhang,¹⁰ Y. L. Zhang,^{3,4} Z. Zhang,¹⁰ Z. Y. Zhang,^{3,4} C. Zhao,^{3,4} H. Y. Zhao,¹² X. F. Zhao,¹³ C. Y. Zhou,¹³ X. Zhu,^{10,††} and Y. Zhu¹³
(DAMPE Collaboration)^{18,‡‡}

X. Luo¹⁸

¹*Dipartimento di Matematica e Fisica E. De Giorgi, Università del Salento, I-73100, Lecce, Italy*

²*Istituto Nazionale di Fisica Nucleare (INFN) - Sezione di Lecce, I-73100, Lecce, Italy*

³*State Key Laboratory of Particle Detection and Electronics,*

University of Science and Technology of China, Hefei 230026, China

⁴*Department of Modern Physics, University of Science and Technology of China, Hefei 230026, China*

⁵*Department of Nuclear and Particle Physics, University of Geneva, CH-1211, Switzerland*

⁶*Gran Sasso Science Institute (GSSI), Via Iacobucci 2, I-67100 L'Aquila, Italy*

⁷*Istituto Nazionale di Fisica Nucleare (INFN) - Laboratori Nazionali del Gran Sasso, I-67100 Assergi, L'Aquila, Italy*

⁸*University of Chinese Academy of Sciences, Beijing 100049, China*

⁹*Particle Astrophysics Division, Institute of High Energy Physics, Chinese Academy of Sciences, Beijing 100049, China*

¹⁰*Key Laboratory of Dark Matter and Space Astronomy,*

Purple Mountain Observatory, Chinese Academy of Sciences, Nanjing 210023, China

¹¹*School of Astronomy and Space Science, University of Science and Technology of China, Hefei 230026, China*

¹²*Institute of Modern Physics, Chinese Academy of Sciences, Lanzhou 730000, China*

¹³*National Space Science Center, Chinese Academy of Sciences, Beijing 100190, China*

¹⁴*Istituto Nazionale di Fisica Nucleare, Sezione di Bari, via Orabona 4, I-70126 Bari, Italy*

¹⁵*Dipartimento di Fisica "M. Merlin", dell'Università e del Politecnico di Bari, via Amendola 173, I-70126 Bari, Italy*

¹⁶*Istituto Nazionale di Fisica Nucleare (INFN) - Sezione di Perugia, I-06123 Perugia, Italy*

¹⁷*Department of Physics and Laboratory for Space Research,*

University of Hong Kong, Hong Kong SAR 999077, China

¹⁸*Shandong Institute of Advanced Technology, Jinan 250100, China*

The Forbush decrease (FD) of cosmic rays is an important probe of the interplanetary environment disturbed by solar activities. In this work, we study the properties of 8 FDs electrons (including positrons) between 2 GeV and 20 GeV from January, 2016 to March, 2024, with the Dark Matter Particle Explorer. The maximum decrease amplitudes of these events are about 30% – 15%, and the amplitudes reduce with energy. The recovery time of these events shows diverse behaviors of their energy-dependence. Some of them show strong energy-dependence, while some have a nearly constant recovery time. It has been shown that such diverse behaviors could be related with the geometry of the disturbed regions of the interplanetary space by coronal mass ejections (CME), represented by the combined effect of the CME velocity, angular spread, and ejection direction.

PACS numbers: 96.25.Qr,98.70.Sa

Introduction. — Galactic cosmic rays (GCRs) are affected by heliospheric plasma and the associated magnetic fields when propagating through the solar system, resulting in flux variations at different time scales (e.g., [1, 2]). One type

of short-time variations, known as Forbush decreases (FDs) [3, 4], is the quick drop and relatively slow recovery of the GCR fluxes over timescales of days to weeks. FDs are caused by energetic solar activities such as coronal mass ejections

(CMEs) [2, 5] or corotating interaction regions (CIRs) [6], which disturb the interplanetary space and block part of GCRs from reaching the detector. Fast CMEs can drive strong interplanetary shocks that also play an important role in generating FDs, such as the two-step FD including an initial decrease by the shock and a further reduction when the CME itself arrives [7]. FDs have also been observed far away from the Earth [8–10], indicating that they are universal phenomenon in the solar system.

FDs are widely studied by ground-based neutron monitors (NMs) or muon detectors (MDs), which measure secondary particles produced by interactions between hadronic GCRs and the atmosphere. The NM or MD data show the integral variations of the GCR intensities above specific energies, which depend on locations of the detectors due to a latitude dependent geomagnetic vertical rigidity cutoff (VRC; [11]). Nonetheless, direct measurements by space experiments, in spite that they are limited by effective areas, provide better composition and energy resolution, and are thus crucial to understanding the physics of FDs. Very few direct measurements of FDs were available, by balloon experiments and space satellites [12–15]. The PAMELA experiment studied FDs of protons, helium nuclei, and electrons, showing charge-sign dependences of their recovery properties [14]. Further investigation of a sample of proton FDs using PAMELA data showed that there are two types of recovery times, type I with significant energy dependence and type II without energy dependence [15]. Similarly, ground-based detectors have identified two distinct types of recoveries [16–18], whose interpretation remains unclear. Using the daily proton fluxes measured by AMS-02 [19], Wang et al. studied the properties of FDs caused by CMEs and CIRs, finding that they do not differ much from each other [20].

Observations of FDs of the leptonic component are even rarer. Daily fluxes of electrons and positrons from May 2011 to November 2021 were published by AMS-02 [21, 22], but no detailed analysis of the FDs has been carried out. An electron FD was reported by PAMELA [14], shows a faster recovery than protons and helium nuclei below 2 GV. The properties of an FD of cosmic ray electrons and positrons (hereafter CREs) were measured by the Dark Matter Particle Explorer (DAMPE) with significantly improved statistics and wide energy coverage, showing clearly energy-dependent recovery times between 2 and 20 GeV [12]. Note that the DAMPE detector itself does not distinguish electrons from positrons due to the lack of magnetic field, and in this work we add electrons and positrons together for the study. The fraction of positrons in the sample is a few percents in our interested energy range [23]. The decrease and recovery behavior observed by DAMPE for this event can be properly accounted for using a diffusion barrier model [12, 24], the more clear underlying physics of FDs needs further exploration using more events. It is an intriguing question whether the recovery times of CRE FDs also experience two types of energy dependence as those of GCR nuclei.

In this work, we analyze the DAMPE CRE data from Jan-

uary 1, 2016 to March 31, 2024 to study the population of FDs. A total of eight large FDs are identified, each with maximum decrease amplitudes exceeding 30% of the average fluxes. The decrease and recovery properties of these events will be investigated in detail.

DAMPE detector. — The DAMPE is a space detector for the observations of cosmic ray nuclei, electrons and positrons, and γ -ray photons [25, 26]. The DAMPE detector is composed of four sub-detectors: a plastic scintillator detector (PSD; [27]) on the top for charge measurement, a silicon-tungsten tracker-converter (STK; [28]) for trajectory and charge measurement, a Bismuth-Germanium-Oxide imaging calorimeter (BGO; [29]) for energy measurement and electron-proton separation, and a neutron detector (NUD; [30]) for auxiliary electron-proton separation. Serving as the key subdetector, the BGO calorimeter consists of 14 layers, each containing 22 bars for a total depth of about $32X_0$ which enables $\sim 1.5\%$ energy resolution for ~ 10 GeV CREs [25]. Different from observing the corona graphs, DAMPE is very suitable for measurements of CREs with a relatively large acceptance of ~ 0.3 m² sr and a high energy resolution. The detector was integrated in a dedicated satellite platform, and was launched into a sun-synchronous orbit at an altitude of 500 km on December 17, 2015 from the Jiuquan base [25].

CRE selection and flux calculation. — The housekeeping system of DAMPE records incident counts of events every 4 seconds, referred to as T_0 counts, to monitor the condition of the data acquisition system [31]. The T_0 trigger rate is a direct measure of the low-energy cosmic ray intensity, which varies from dozens Hz near the equator to tens of thousands Hz at the poles. Simulations indicate that T_0 triggering occurs when the energy of a particle is higher than 100 MeV. FD candidates are selected using the DAMPE T_0 rate and the OULU NM count rate, both exhibit a rapid decrease plus a relatively slow recovery. Specifically, if the DAMPE T_0 rate decreases by more than 10% and the OULU NM count rate decreases over 3% within 3 days, the corresponding time window is labelled as a possible FD event occurs. Then a cross match with the SOHO LASCO CME catalog¹ is further required. In total we find 8 candidate FDs according to this procedure. The basic information of these 8 FD events can be found in Table S1 of the Supplemental Material. For each candidate event, we select data from 10 days before to 30 days after the starting time for the follow-up analysis. CRE candidates are selected following the method described in Ref. [12]. Data recorded during the passage of the South Atlantic Anomaly (SAA) region are excluded. Both events passing the high-energy trigger (HET) and low-energy trigger (LET) [31] conditions are used. The reconstructed particle charge [32] is set to be $Z \leq 1.7$, which rejects $\sim 99\%$ of nuclei heavier than protons. We further require that the shower maximum is not at the edge of the first six BGO layers, and the reconstructed track

¹ https://spase-metadata.org/NASA/Catalog/SOHO/LASCO/CME_Catalog.html

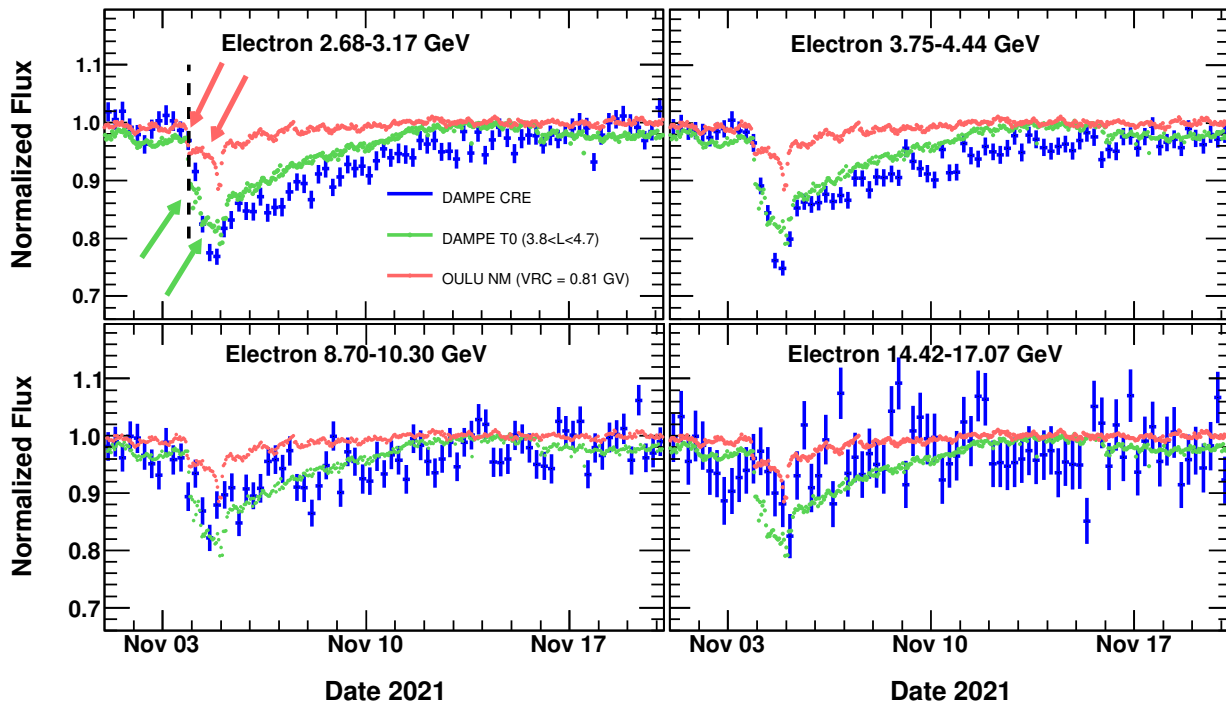


FIG. 1: Time profiles of CRE fluxes in four energy bins measured by DAMPE in November, 2021 (blue dots), compared with the DAMPE T_0 rate (green curves) and OULU NM data (red curves). The errorbars of the DAMPE CRE fluxes include both the statistical uncertainties and systematic uncertainties, added in quadrature. The 4 panels correspond to 4 different CRE energy bins as labelled. Arrows in the top-left panel show the two step decreases revealed by the NM data and DAMPE T_0 data, and the black dashed line shows the arrival time of the interplanetary shock.

is required to penetrate the first four BGO layers. The pre-selection efficiency is shown in Fig. S1 of the Supplemental Material. We can see that the efficiency reaches about 80% for energies higher than a few GeV. At low energies the efficiency drops quickly, due mainly to the trigger efficiency.

After these pre-selections, the main background for CREs is protons. We use a particle identification (PID) parameter, defined as $PID = F(E)[\log(R_r) \cdot \sin \theta + \log(R_l) \cdot \cos \theta]$ to distinguish CREs from protons, where $F(E)$ is an energy decoupling polynomial, θ is a rotation angle, R_r and R_l are parameters describing the radial and longitudinal extensions of the shower in the calorimeter [12]. Fig. S2 of the Supplemental Material illustrates the distributions of the PID parameter for two energy bins, 3.17 – 3.44 GeV and 7.35 – 8.00 GeV. CREs would typically have $PID \leq 2$. To properly estimate the proton background, we carry out a fit to the data with Monte Carlo (MC) simulation templates of CREs and protons. Since CMEs affect electrons and protons differently [14], the background is estimated independently for each energy and time bin. We find that the proton background is about 2% to 8% for energies from 2 to 20 GeV, with about 15% relative changes (differ case by case) during the FD period.

The CRE flux is calculated as

$$I_{i,j} = \frac{N_{i,j}}{\Delta E_i A_i T_{i,j} \eta_i}, \quad (1)$$

where $N_{i,j}$ is the number of selected CREs after the background subtraction in the i th energy bin and j th time bin, $T_{i,j}$ is the corresponding exposure time, ΔE_i is the energy bin width, A_i is the geometric acceptance, and η_i is the total efficiency. To avoid the shielding effect from the geomagnetic field, we require that the particle's rigidity is higher than 1.2 times of the VRC values. Since the VRC value varies with latitude, the rigidity threshold results in variations of the exposure time with time and energy (see Fig. S3 of the Supplemental Material). On average, the effective exposure time is approximately 80% of the total time for energies above 15 GeV, and decreases gradually to about 30% at 2 GeV.

Since we focus on the relative change of the CRE fluxes at a time scale of about one month, the main systematic uncertainties are the efficiency stabilities. The efficiency fluctuation is estimated to be $< 0.15\%$ within one month after correcting the temperature effect [33]. It has also been shown that there is a long-term evolution of the trigger efficiency due to radiation damage, electronics aging, and gain decrease of photomultipliers, which results in a decrease of the HET efficiency by

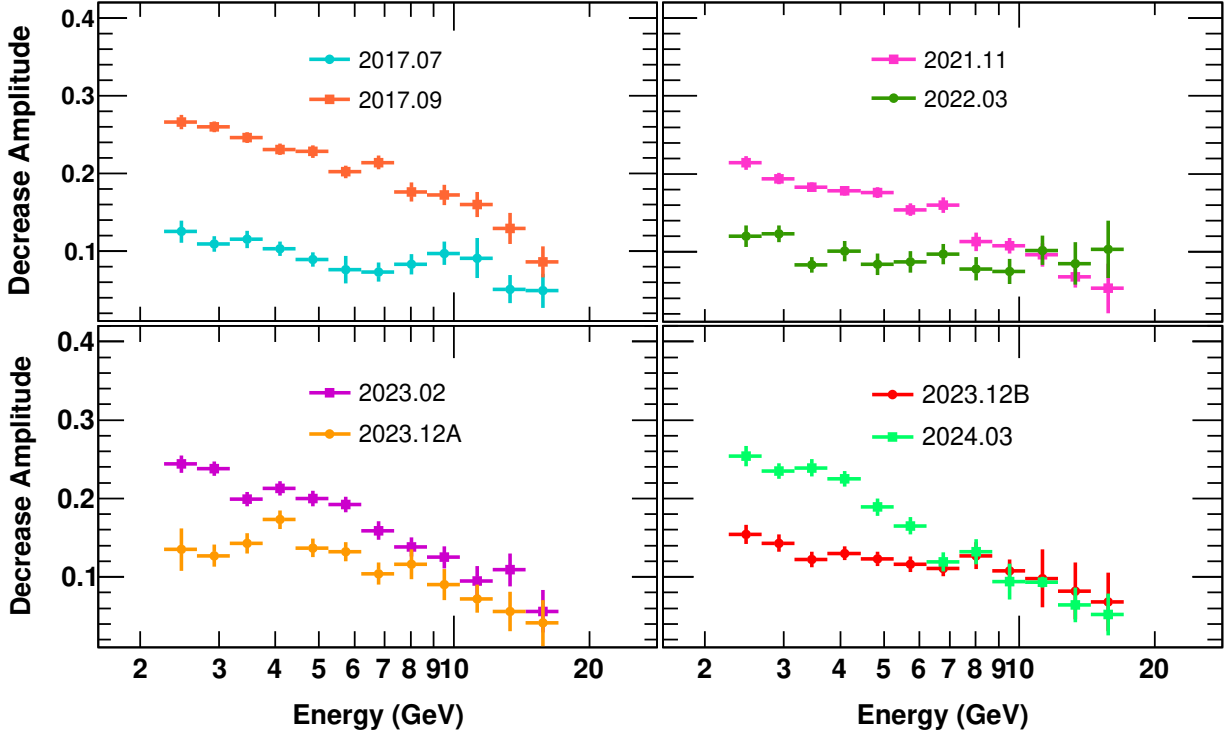


FIG. 2: The decrease amplitude as a function of energy, for the eight FDs observed by DAMPE.

about 5% per year at 2 GeV and smaller with increasing energies [34]. The systematic uncertainties are much smaller than the statistical uncertainties, which are about 3% at 2 GeV and about 7% at 20 GeV.

Results of FDs. — Fig. 1 shows the measured CRE fluxes with a time resolution of 6 hours in 4 energy bins for the FD event in November, 2021. Also shown are the NM data from the OULU station (red), and T_0 count rate of DAMPE (green) for the McIlwain L-values [35] of 3.8 – 4.7 which roughly corresponds to the VRC value of the OULU NM station. The fluxes 20 days prior to the FD are used as reference for normalizations. Note that, although the cutoff rigidities of the OULU station and the DAMPE T_0 events are similar, they represent essentially different particle energies since NMs record secondary neutrons produced by cosmic rays with much higher energies. This explains the differences of their decrease amplitudes.

As can be found from Fig. 1, the CRE fluxes experience a fast decrease at UT 21:00 on November 3, 2021, reach the minimum at UT 21:00 on November 4, and gradually recover to the normal level in about 2 weeks. The T_0 rate follows a trend similar to that of CRE fluxes. Different from the September 2017 event [12], no precursor was observed for in this event. The NM profile reaches its minimum at similar time as the T_0 count rate, but is about 3 hours later than the minimum time of the CRE fluxes. The NM profile also shows

a faster recovery (with characteristic timescale of ~ 2 days) than the CRE fluxes and the T_0 count rate (with characteristic timescale of ~ 4.5 days). Both the NM and the DAMPE T_0 data experience two-step decrease features, as marked by arrows. Possible explanations of the two-step features could be found in Ref. [36]. We note that the T_0 rate exhibits a larger decrease amplitude in the first step and a smaller amplitude in the second step, in contrary to those of NM data. Such differences may again be due to different energies. The time profiles for other events can be found in Fig. S6 of the Supplemental Material.

The recovery phase of the FD is important in revealing the properties of the interplanetary environment disturbed by the CME. The following function is employed to fit the recovery profile of an FD:

$$\frac{I_t}{I_0} = 1 - A_e \exp\left(-\frac{t - t_m}{\tau}\right), \quad (2)$$

where I_t is the measured CRE flux at time t , I_0 is the normalization flux before the FD, A_e is the decrease amplitude, t_m is the time of minimum, and τ is the characteristic recovery time.

The derived decrease amplitudes and recovery times, for each energy bin, are shown in Fig. 2 and Fig. 3. Note that when performing the fitting, the systematic uncertainties are conservatively included via a quadratic sum with the statistical uncertainties. The decrease amplitude becomes smaller

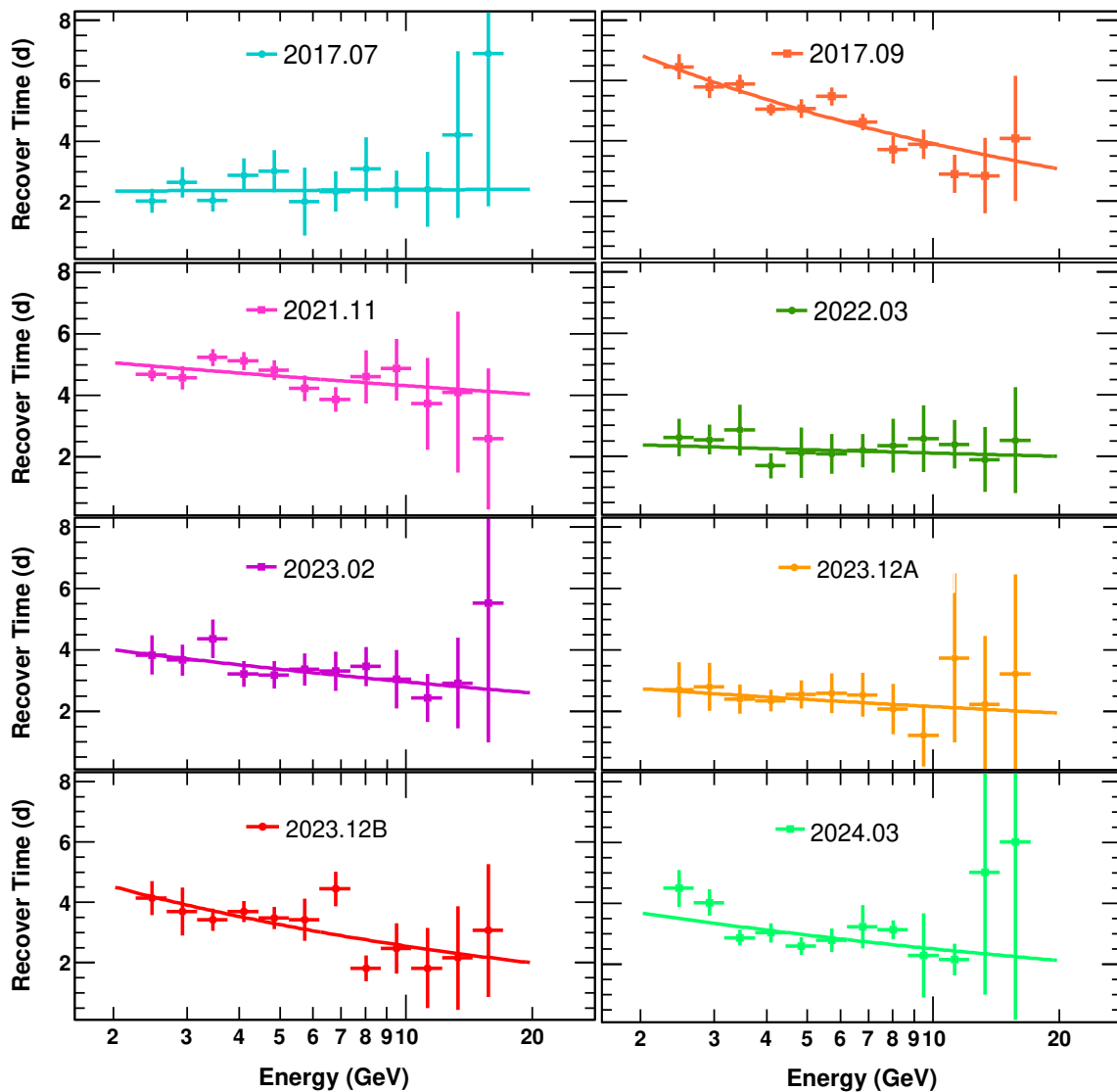


FIG. 3: The recover time as a function of energy, for the eight FD observed by DAMPE. The solid line in each panel shows the best-fit power-law result.

with the increasing energy. This can be explained by the fact that particles with higher energy are less affected by the magnetic turbulence. The energy dependence of the recovery time, however, shows diverse properties. For some events, the recovery time becomes shorter with the increase of energy (e.g., the 2017-09 event), while for others it remains nearly constant for all energies (e.g., the 2017-07 event). These diverse behaviors may be related with properties of CMEs causing the FDs. We further fit the energy dependence of the recovery time with a power-law function, $\tau = aE^b$, and derive the power-law index b for each event. The results of the parameter b for the 8 events are shown in Fig. 4.

To investigate the behaviors of the recovery time, we also show in Fig. 4 the possible relation between b and a combined parameter, $V_{\text{CME}} \cdot \Omega$, for these events. The CME velocity V_{CME} reflects the strength of the disturbance, and Ω is the solid

angle of the CME which reflects the spatial size affected by the CME. The CME parameters are extracted from the Wang-Sheeley-Argue (WSA)-Enlil solar wind prediction model² [37–39]. The model reconstructs the CME speed (V_{CME}) and the solid angle (Ω) in a region of 5 to 20 solar radii using corona graphs from three different satellites, including STEREO-B COR2, STEREO-A COR2, and LASCO C2. The projection effect has been taken into account. Another potentially important parameter affecting the FDs of GCRs is the ejection direction of the CME [18]. We classify the CMEs into head-on events (I), glancing events (III), and intermediate events (II) (see Fig. S5 of the Supplemental Material for a schematic

² <https://www.swpc.noaa.gov/products/wsa-enlil-solar-wind-prediction>

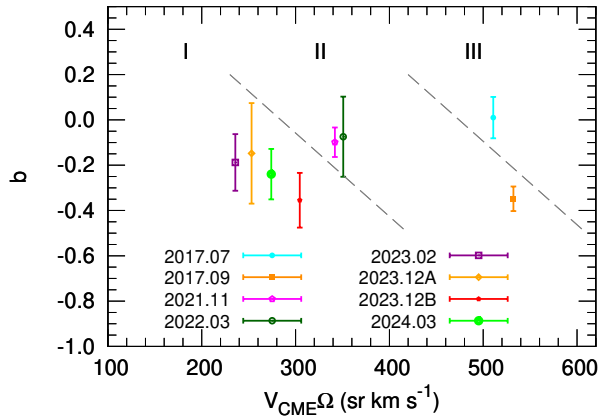


FIG. 4: Possible relationship between b and $V_{\text{CME}} \cdot \Omega$ as revealed by the DAMPE detected FDs. The dashed lines divide the CMEs schematically into head-on events (I), glancing events (III), and intermediate ones (II).

plot of the classification). Note that the boundaries among these categories are not sharply defined, and the current classification is just for illustrative purpose. As can be seen in Fig. 4, for classes I and II events, anti-correlations between the slope b and $V_{\text{CME}} \cdot \Omega$ is observed. Only one class III FD event has been detected at present, and the relationship between b and $V_{\text{CME}} \cdot \Omega$ is not clear yet. An exception is the March 2022 event, which should be classified as a head-on event based on the CME parameters (see Table S1 of the Supplemental Material), but its (b , $V_{\text{CME}} \cdot \Omega$) values place it in region II as labelled in Fig. 4. The precise classification of this event is ambiguous since the decrease amplitude is small, leading to a relatively large uncertainty of the slope parameter b . Roughly, stronger CMEs (faster in speed and wider in spread) would result in stronger energy dependence of the recovery time.

The transport of a charged particle in the heliosphere can be described by the Parker's equation [40] (see the Supplemental Material). CMEs and other solar activities may disturb the interplanetary space, leading to perturbation of the propagation of GCRs. This process can be modeled by a fast-moving diffusion barrier [24]. More details about the setting of the diffusion barrier can be found in the Supplemental Material. We adopt the stochastic differential equation (SDE) method to solve Parker's equation with the disturbance by CMEs [41, 42]. In the modeling, the basic parameters of the CMEs, such as the velocity, angular extension, and direction, are from the WSA-ENLIL model. The other parameter is the diffusion coefficient inside the barrier, which is adjusted to fit the measurements. As shown in Fig. S6 of the Supplemental Material, the time profiles of the CRE fluxes around the FDs can be reproduced by this model. The comparison of the energy-dependence slope parameter b of the recovery time between DAMPE observations and simulations is given in Fig. S7 of the Supplemental Material, which also shows a good consistency. The simulation indi-

cates that the recovery behaviors of FDs depend on multiple factors, including the motion and geometry of the disturbed regions. Thus the diverse properties of the CRE FDs observed by DAMPE reflect the complicated propagation processes of particles in the interplanetary space. Note further that, the FD events reported in this analysis occurred between 2017 and 2024, during which the solar magnetic polarity was always positive³ ($A > 0$). We have a consistent drift direction configuration for all events, isolating the additional complexity due to the polarity reversal.

Conclusion. — In this work we study the FDs of CREs recorded by DAMPE, from January, 2016 to March, 2024. Different from most of existing studies which focus on the nuclear component of GCR FDs, this is the first systematic investigation of FDs of the electron and positron component. In the total 8 FD events detected, the largest decrease amplitude reaches about 30%. The energy dependence of the decrease amplitude and recovery time, from 2 GeV to 20 GeV, is well measured. We find that the energy dependence of the recovery time show diverse behaviors, which span from strongly energy-dependent to nearly energy-independent. Our results further suggest that this diversity is likely due to a combined effect of the CME velocity, angular extension, and propagation direction. Depending on the ejection direction of the CME relative to the Earth, an anti-correlation between the energy dependence slope of the recovery time and the velocity times solid angle of the CME is revealed by the data. Utilizing a diffusion barrier model, we can account for the measurements under the framework of Parker's transport equation, based on observed parameters of the CMEs.

With the sunspot number approaching its maximum during the solar cycle 25, more FD events are expected to be detected, which will be very helpful in testing the phenomenae found in this study. Particularly, additional events belonging to with classes II and III will be especially important. Furthermore, the comparative studies of FDs of CREs and protons or other nuclei, as in Ref. [14] but with a significantly enlarged sample are of great interest and will be carried out in future works. Finally, the joint analysis of the FD events and the sun shadow by groundbased cosmic ray experiments [43] will be crucial in improving our understanding of impacts of solar activities on the interplanetary magnetic environment and the particle propagation in the heliosphere.

The data that support the findings of this article are openly available⁴.

³ A positive solar magnetic polarity corresponds to an outward-pointing heliospheric magnetic field in the Sun's northern hemisphere and an inward-pointing magnetic field in the southern hemisphere.

⁴ <https://doi.org/10.57760/sciencedb.space.02998>

Acknowledgments

The DAMPE mission was funded by the strategic priority science and technology projects in space science of Chinese Academy of Sciences (CAS). In China, the data analysis is supported by the National Key Research and Development Program of China (No. 2022YFF0503302), the National Natural Science Foundation of China (Nos. 12220101003 and 12321003), the CAS Project for Young Scientists in Basic Research (No. YSBR-061), and the Youth Innovation Promotion Association of CAS. In Europe, the activities and data analysis are supported by the Swiss National Science Foundation (SNSF), Switzerland, the National Institute for Nuclear Physics (INFN), Italy, and the European Research Council (ERC) under the European Union's Horizon 2020 research and innovation programme (No. 851103).

* Now at Institute of Physics, Ecole Polytechnique Fédérale de Lausanne (EPFL), CH-1015 Lausanne, Switzerland.

† Also at Dipartimento di Fisica e Geologia, Università degli Studi di Perugia, I-06123 Perugia, Italy.

‡ Now at Dipartimento di Fisica e Chimica “E. Segrè”, Università degli Studi di Palermo, via delle Scienze ed. 17, I-90128 Palermo, Italy.

§ Now at Inter-university Institute for High Energies, Université Libre de Bruxelles, B-1050 Brussels, Belgium.

¶ Now at New York University Abu Dhabi, Saadiyat Island, Abu Dhabi 129188, United Arab Emirates.

** Also at School of Physics and Electronic Engineering, Linyi University, Linyi 276000, China.

†† Also at School of computing, Nanjing University of Posts and Telecommunications, Nanjing 210023, China.

‡‡ Electronic address: dampe@pmo.ac.cn

- [1] M. S. Potgieter, *Living Reviews in Solar Physics* **10**, 3 (2013), 1306.4421.
- [2] H. V. Cane, *Space Sci. Rev.* **93**, 55 (2000).
- [3] S. E. Forbush, *Physical Review* **51**, 1108 (1937).
- [4] V. F. Hess and A. Demmelmair, *Nature* **140**, 316 (1937).
- [5] X. X. Yu, H. Lu, G. M. Le, and F. Shi, *Solar Physics* **263**, 223 (2010).
- [6] B. Heber, T. R. Sanderson, and M. Zhang, *Advances in Space Research* **23**, 567 (1999).
- [7] A. P. Jordan, H. E. Spence, J. B. Blake, and D. N. A. Shaul, *Journal of Geophysical Research (Space Physics)* **116**, A11103 (2011).
- [8] J. Guo, et al., *Astron. Astrophys.* **611**, A79 (2018), 1712.06885.
- [9] L. F. Burlaga, F. B. McDonald, and N. F. Ness, *J. Geophys. Res.* **98**, 1 (1993).
- [10] M. Armano, et al., *Astrophys. J.* **874**, 167 (2019), 1904.04694.
- [11] D. F. Smart and M. A. Shea, *Advances in Space Research* **36**, 2012 (2005).
- [12] F. Alemanno, et al., *Astrophys. J. Lett.* **920**, L43 (2021), 2110.00123.
- [13] P. Meyer and R. Vogt, *J. Geophys. Res.* **66**, 3950 (1961).
- [14] R. Munini, et al., *Astrophys. J.* **853**, 76 (2018), 1803.06166.
- [15] I. A. Lagoida, et al., *Solar Physics* **298**, 9 (2023).
- [16] T. Jämsén, I. G. Usoskin, T. Rähkä, J. Sarkamo, and G. A. Kovaltsov, *Advances in Space Research* **40**, 342 (2007).
- [17] I. G. Usoskin, I. Braun, O. G. Gladysheva, J. R. Hörandel, T. Jämsén, G. A. Kovaltsov, and S. A. Starodubtsev, *Journal of Geophysical Research (Space Physics)* **113**, A07102 (2008).
- [18] L. L. Zhao and H. Zhang, *Astrophys. J.* **827**, 13 (2016).
- [19] M. Aguilar, et al., *Phys. Rev. Lett.* **127**, 271102 (2021).
- [20] S. Wang, V. Bindi, C. Consolandi, C. Corti, C. Light, N. Nikonov, and A. Kuhlman, *Astrophys. J.* **950**, 23 (2023).
- [21] M. Aguilar, et al., *Phys. Rev. Lett.* **130**, 161001 (2023).
- [22] M. Aguilar, et al., *Phys. Rev. Lett.* **131**, 151002 (2023).
- [23] M. Aguilar, et al., *Phys. Rev. Lett.* **110**, 141102 (2013).
- [24] X. Luo, M. S. Potgieter, M. Zhang, and X. Feng, *Astrophys. J.* **860**, 160 (2018).
- [25] J. Chang, et al., *Astroparticle Physics* **95**, 6 (2017), 1706.08453.
- [26] DAMPE Collaboration, et al., arXiv e-prints arXiv:2511.05409 (2025), 2511.05409.
- [27] Y. Yu, et al., *Astroparticle Physics* **94**, 1 (2017), 1703.00098.
- [28] P. Azzarello, et al., *Nuclear Instruments and Methods in Physics Research A* **831**, 378 (2016).
- [29] Y.-L. Zhang, et al., *Chinese Physics C* **36**, 71 (2012).
- [30] Y.-Y. Huang, T. Ma, C. Yue, Y. Zhang, M.-S. Cai, J. Chang, T.-K. Dong, and Y.-Q. Zhang, *Research in Astronomy and Astrophysics* **20**, 153 (2020), 2005.07828.
- [31] Y.-Q. Zhang, J.-H. Guo, Y. Liu, C.-Q. Feng, Y.-L. Zhang, T.-K. Dong, J.-J. Zang, and C. Yue, *Research in Astronomy and Astrophysics* **19**, 123 (2019).
- [32] T. Dong, et al., *Astroparticle Physics* **105**, 31 (2019), 1810.10784.
- [33] G. Ambrosi, et al., *Astroparticle Physics* **106**, 18 (2019), 1907.02173.
- [34] W.-H. Li, C. Yue, Y.-Q. Zhang, J.-H. Guo, and Q. Yuan, *Nuclear Instruments and Methods in Physics Research A* **1069**, 169815 (2024), 2409.03352.
- [35] M. Walt, *Camb. Atmos. Space Sci. Ser* **10** (1994).
- [36] S. O. Ifedili, *Journal of Geophysical Research (Space Physics)* **109**, A02117 (2004).
- [37] Y. M. Wang and N. R. Sheeley, Jr., *Astrophys. J.* **355**, 726 (1990).
- [38] C. N. Arge, D. Odstrcil, V. J. Pizzo, and L. R. Mayer, in *Solar Wind Ten*, edited by M. Velli, R. Bruno, F. Malara, and B. Bucci (AIP, 2003), vol. 679 of *American Institute of Physics Conference Series*, pp. 190–193.
- [39] G. Millward, D. Biesecker, V. Pizzo, and C. A. de Koning, *Space Weather* **11**, 57 (2013).
- [40] E. N. Parker, *Planet. Space Sci.* **13**, 9 (1965).
- [41] R. D. Strauss, M. S. Potgieter, I. Büsching, and A. Kopp, *Astrophys. J.* **735**, 83 (2011).
- [42] M. Zhang, *Astrophys. J.* **513**, 409 (1999).
- [43] The LHAASO Collaboration, C. W. Jiang, and Y. Yang, *The Innovation* **5**, 100695 (2024), 2410.09064.
- [44] J. R. Jokipii, E. H. Levy, and W. B. Hubbard, *Astrophys. J.* **213**, 861 (1977).
- [45] R. A. Burger and M. S. Potgieter, *Astrophys. J.* **339**, 501 (1989).
- [46] X. Luo, M. S. Potgieter, V. Bindi, M. Zhang, and X. Feng, *Astrophys. J.* **878**, 6 (2019), 1909.03050.
- [47] C.-R. Zhu, Q. Yuan, and D.-M. Wei, *Astroparticle Physics* **124**, 102495 (2021), 2007.13989.

Supplemental Material of “Diverse properties of electron Forbush decreases revealed by the Dark Matter Particle Explorer”

(The DAMPE collaboration)

PROPERTIES OF 8 CRE FDS AND THE ASSOCIATED CMES

Table S1 gives the main parameters of the 8 FDs discussed in this work, including the DAMPE measured CRE fluxes, the CME parameters from the WSA-ENLIL model, and the parameters of the diffusion barrier used in our simulation.

TABLE S1: Main parameters of the 8 FDs. From left to right, they are, the time at which the DAMPE T_0 rate reaches the minimum (Time), the maximum decrease amplitude of DAMPE CRE fluxes (A_e^{\max}), the recover time of DAMPE CRE at 2.3 GeV (τ), the slope of energy dependence of recover time (b), the CME speed (V_{CME}), the half angle width of CME (Θ), the reduction factor of the diffusion coefficient in the barrier (ρ), the location of the Earth in the CME coordinate (θ_0, ϕ_0), the latitude and longitude angular widths of CME ($\theta_{\text{br}}, \phi_{\text{br}}$). The symbol in parenthesis after ϕ_0 gives the classification of the event as defined in this work.

DAMPE CRE Observations				CME Parameters		Simulation Parameters				
Time (UTC)	A_e^{\max}	τ (day)	b	V_{CME} (km s $^{-1}$)	Θ ($^\circ$)	ρ	θ_0 ($^\circ$)	ϕ_0 ($^\circ$)	θ_{br} ($^\circ$)	ϕ_{br} ($^\circ$)
2017-07-17 04:30	0.125 ± 0.014	2.03 ± 0.39	0.010 ± 0.091	1199	57	4.25	70	-50 (III)	100	120
2017-09-08 13:30	0.266 ± 0.009	6.46 ± 0.42	-0.348 ± 0.054	1611	48	8.25	90	45 (II)	90	120
2021-11-04 21:30	0.214 ± 0.009	4.69 ± 0.24	-0.099 ± 0.065	1397	41	7.00	90	30 (II)	90	90
2022-03-14 19:30	0.123 ± 0.014	2.61 ± 0.61	-0.074 ± 0.018	983	50	6.50	100	0 (I)	100	100
2023-02-28 14:30	0.244 ± 0.011	3.83 ± 0.64	-0.187 ± 0.125	1237	36	5.00	90	0 (I)	60	80
2023-12-01 18:30	0.137 ± 0.027	2.72 ± 0.89	-0.148 ± 0.222	944	43	5.50	90	0 (I)	90	90
2023-12-17 22:30	0.154 ± 0.012	4.15 ± 0.56	-0.355 ± 0.121	921	48	7.25	90	10 (I)	100	90
2024-03-24 22:30	0.254 ± 0.013	4.49 ± 0.60	-0.239 ± 0.111	1438	36	10.0	100	0 (I)	90	80

PRE-SELECTION EFFICIENCY

The pre-selections include the trigger selection, the charge selection, the track selection, and the shower containment requirement. The selection efficiency as a function of energy is shown in Fig. S1.

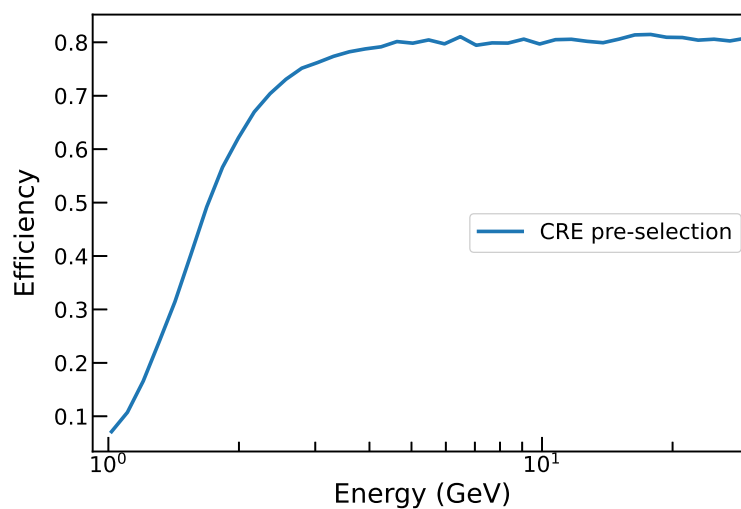


FIG. S1: The CRE pre-selection efficiency as a function of reconstructed energy.

BACKGROUND SUBTRACTION

After pre-selections, the data sample includes mainly CREs and protons. To distinguish CREs from the proton background, a particle identification (PID) variable is defined [12] to describe the shower development in the calorimeter. Fig. S2 shows the PID distributions in two energy bins. Curves in red and green are MC simulated PID distributions of CREs and protons, and the blue ones are the sum of these two components, obtained by a fit to the data using the MC templates. The proton contamination is then obtained and subtracted from the data sample.

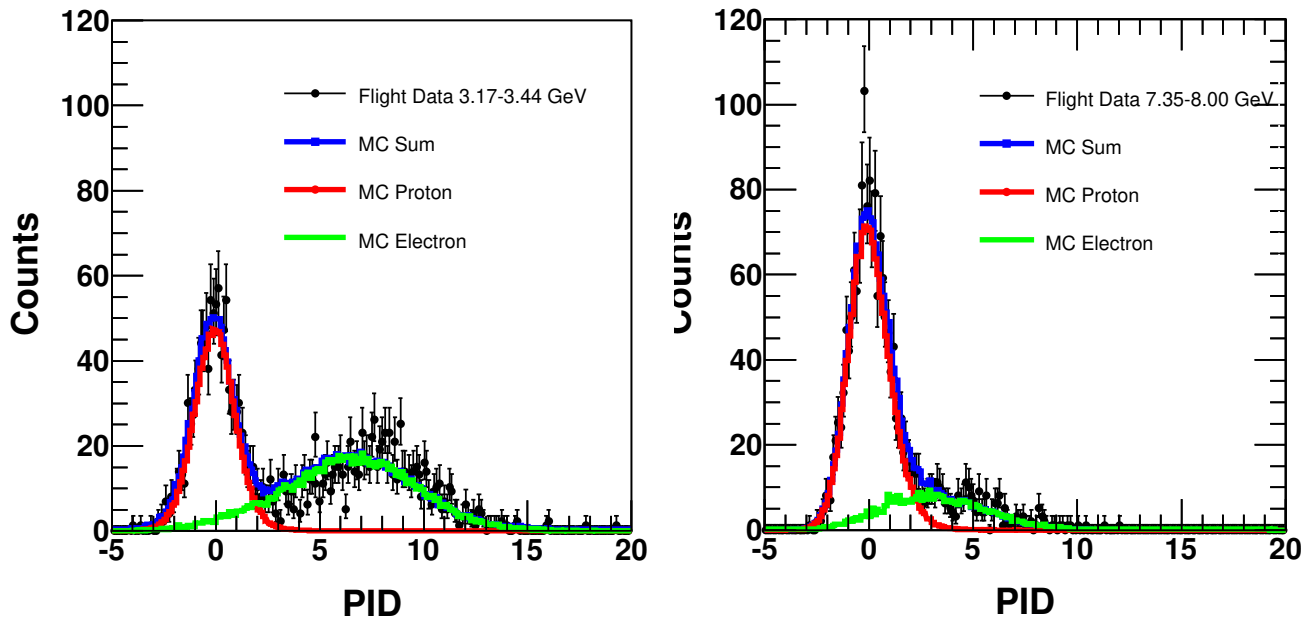


FIG. S2: The PID distributions of the flight data (black dots) and MC simulations (red for electrons, green for protons, and blue for their sum). The left panel is for the energy bin of 3.17 – 3.44 GeV, and the right panel is for the energy bin of 7.35 – 8.00 GeV.

EXPOSURE CORRECTION AT LOW ENERGIES

Due to the geomagnetic field, low energy CRs will get shielded and can not reach the orbit of DAMPE. This corresponds to a cutoff of the low energy spectrum of particles. To avoid the impact of the cutoff effect, a threshold of the particle rigidity of 1.2 times of the VRC value is set, which results in latitude-dependent (and consequently time-dependent) and energy-dependent exposure time. For each energy and time interval, the exposure time is calculated as the sum of the satellite travel time when this given rigidity satisfies the above threshold condition. The time when the satellite passes through the South Atlantic Anomaly (SAA) region, when the instrument switches to the calibration mode, and the dead time of the data acquisition system, is also excluded. Fig. S3 shows an illustration of the exposure time from 2 GeV to 20 GeV for the time from November 1 to November 31, 2021. We can see that the exposure time is almost constant above 12 GeV, and decreases at lower energies due to the geomagnetic cutoff effect.

ELECTRON TRANSPORT IN THE HELIOSPHERE

The transport of particles in the heliosphere is described by the Parker's equation [40]:

$$\frac{\partial f}{\partial t} = -(\vec{V}_{sw} + \langle \vec{V}_d \rangle) \cdot \nabla f + \nabla \cdot (K^{(s)} \cdot \nabla f) + \frac{1}{3}(\nabla \cdot \vec{V}_{sw}) \frac{\partial f}{\partial \ln p}, \quad (3)$$

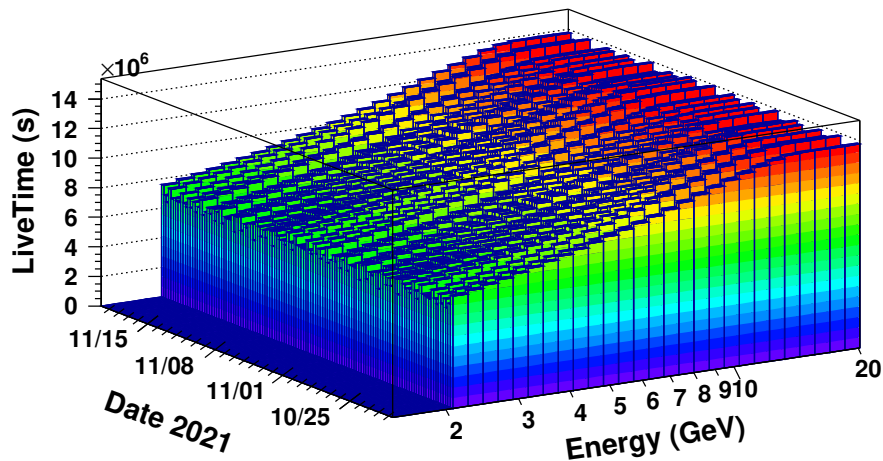


FIG. S3: Exposure time of DAMPE as a function of time and energy.

where $f(\vec{r}, p, t)$ is the particle distribution function, p is momentum, \vec{V}_{sw} is the latitude-dependent solar wind speed, $\langle \vec{V}_d \rangle$ is the pitch-angle averaged drift velocity which has the following form [44, 45]

$$\langle \vec{V}_d \rangle = \frac{pv}{3q} \nabla \times \frac{\vec{B}}{B^2}, \quad (4)$$

where q and v are charge and velocity of GCR particles, and \vec{B} is the interplanetary magnetic field (IMF). The variable $K^{(s)}$ is the symmetric diffusion tensor, aligned in the IMF coordinate, whose diagonal components are the parallel diffusion coefficient K_{\parallel} , and the perpendicular diffusion coefficients $K_{\perp\theta}$ and $K_{\perp r}$.

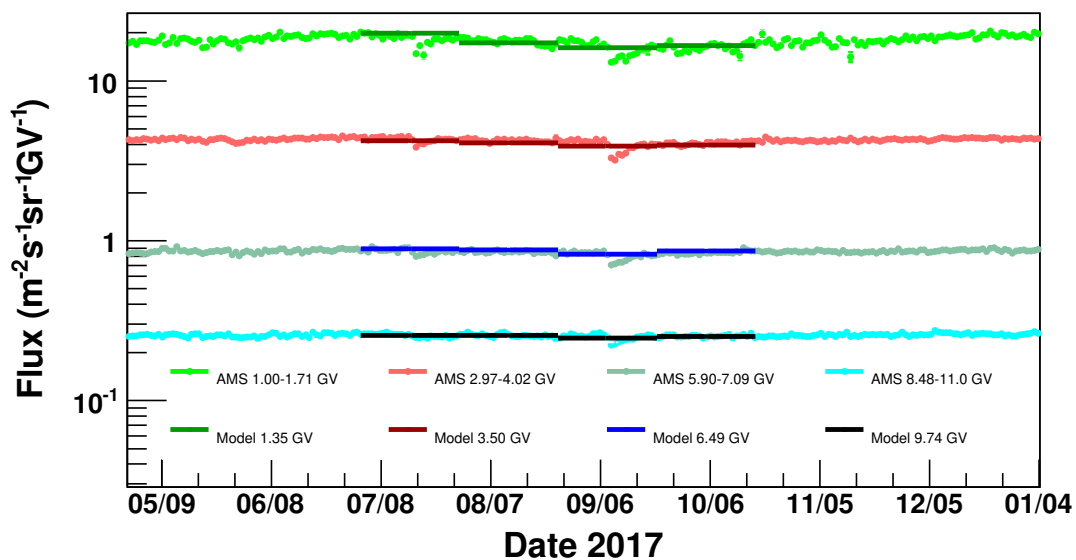


FIG. S4: Simulation of the solar modulation effect on electrons, compared with the AMS-02 daily electron fluxes [21], for Bartel rotations from 2509 to 2512 in 2017.

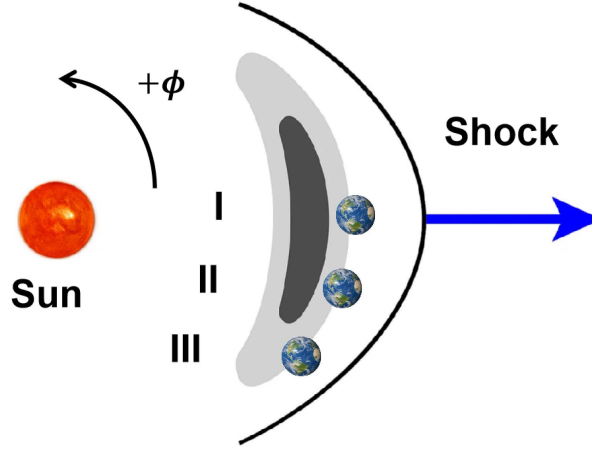


FIG. S5: Schematic plot to show the relative location of the Earth in the CME for the three types of events.

In this work the diffusion coefficients are parameterized as [46])

$$K_i = K_{i0} \beta \frac{B_0}{B} \left(\frac{P}{P_k} \right)^a \left[1 + \left(\frac{P}{P_k} \right)^{\frac{b-a}{c}} \right]^c, \quad (5)$$

where i represents \parallel , $\perp\theta$, or $\perp r$; β is the particle velocity in speed of light, B is the strength of the IMF, $B_0 \equiv 1$ nT, K_{i0} is the normalization diffusion coefficient varying with time, p_k is the break momentum of the diffusion coefficient, a , b are the power-law indices before and after the break, and c characterizes the smoothness of the break.

The IMF is described by the standard Parker field as

$$\vec{B}(r, \theta) = \frac{AB_\oplus}{r^2} \left(\hat{e}_r - \frac{r\Omega \sin \theta}{V_{sw}} \hat{e}_\theta \right) [1 - 2H(\theta - \theta_{cs})], \quad (6)$$

where B_\oplus is an average of 13 months magnetic field strength before the specific time at 1 AU, A describes the polarity of the IMF, defined as $A = \pm 1 / \sqrt{1 + (\Omega/V_{sw})^2}$, θ_{cs} determines the polar extent of the Heliospheric Current Sheet (HCS), and Ω is the angular velocity of the sun.

The Parker's equation is solved numerically with the stochastic differential equation (SDE) technique [41, 42]. The parameters of the diffusion coefficient are derived through fitting the electron fluxes measured by AMS-02 [21], using the local interstellar spectrum of electrons derived in Ref. [47] (see Fig. S4 for an example of the model fitting results in 2017). The relatively small portion of positrons has been omitted in the calculation.

THE DIFFUSION BARRIER MODEL OF FD

The CME is described by a three dimensional diffusion barrier, in which the diffusion coefficient is smaller than the interplanetary value [24]. The diffusion coefficient inside the barrier is written as

$$K'_i = \frac{K_i}{1 + \rho h(\theta) f(r) g(\phi)}, \quad (7)$$

where ρ is the reduction factor, $h(\theta)$, $g(\phi)$, and $f(r)$ describes the geometry of the diffusion barrier, as

$$h(\theta) = e^{-\left(\frac{\theta - \theta_0}{\theta_{br}}\right)^{10}}, \quad (8)$$

$$g(\phi) = e^{-\left(\frac{\phi - \phi_0}{\phi_{br}}\right)^{10}}, \quad (9)$$

$$f(r) = \begin{cases} 1 - \frac{r - r_{\text{cen}}}{r_a}, & r_{\text{cen}} < r < r_{\text{fr}} \\ \frac{r - r_{\text{end}}}{r_b}, & r_{\text{end}} < r \leq r_{\text{cen}} \\ 0, & \text{others} \end{cases}, \quad (10)$$

where (θ_0, ϕ_0) are the direction of the CME center. For $\theta_0 = \pi/2$ and $\phi_0 = 0$, the CME hits the Earth head on. Parameter θ_{br} and ϕ_{br} describes the extension of the barrier. The radical location of the front, center, and end of the CME are depicted as r_{fr} , r_{cen} , and r_{end} , and the widths of the leading and trailing parts of the barrier are $r_a = r_{\text{fr}} - r_{\text{cen}}$ and $r_b = r_{\text{cen}} - r_{\text{end}}$. The same SDE method is employed to calculate the time-dependent electron fluxes including the diffusion barrier. The parameters used to fit the DAMPE data are given in Table S1. A comparison between the observed time profiles and simulated ones for the 8 FDs is shown in Fig. S6. We also fit the slopes of the energy-dependence of the recovery time for the simulation results, which are shown in Fig. S7 with a comparison with observations. Here the uncertainties of b_{Simu} are obtained through scaling down the simulation sample to similar event statistics with the flight data, which makes the comparison between the observations and simulations more direct.

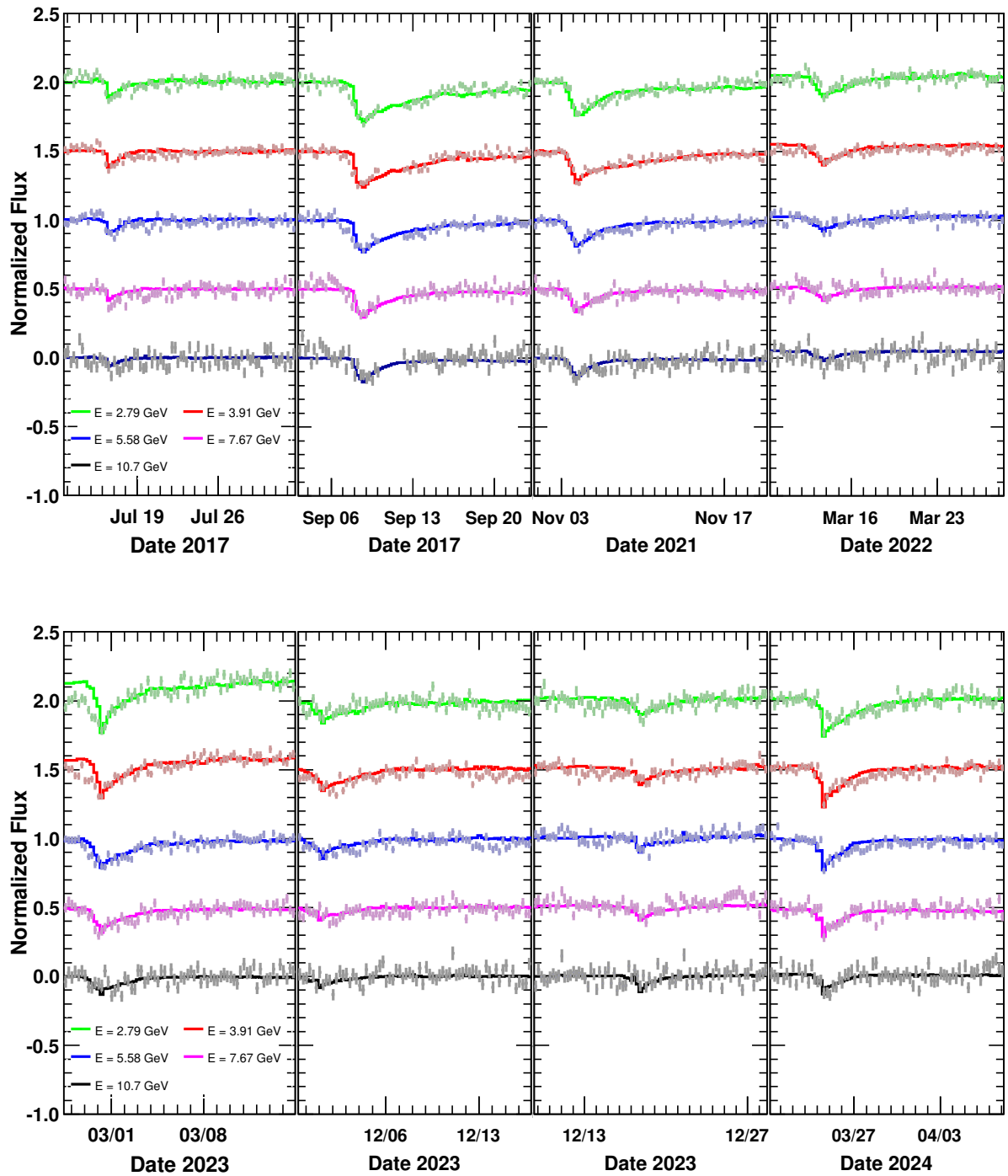


FIG. S6: Comparison of the DAMPE observed CRE time profiles (dots) with the simulation results (lines) for 5 selected energy bins.

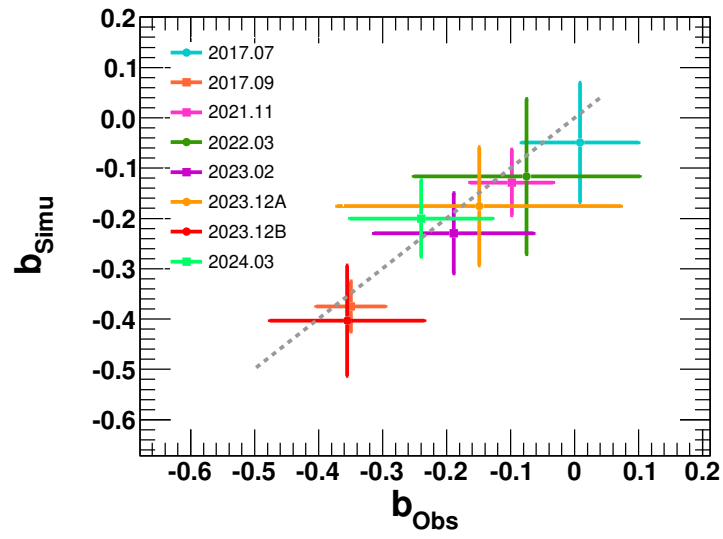


FIG. S7: The slope parameter b derived from DAMPE observations (b_{Obs}) and simulations (b_{Simu}).